

Interfacial dripping faucet: generating monodisperse liquid lenses

Lorène Champougny^{1,2}, Vincent Bertin³, Jacco H. Snoeijer³, and Javier Rodríguez-Rodríguez^{1,2}

¹Department of Thermal and Fluids Engineering, Carlos III University of Madrid, Spain

²Instituto Gregorio Millán, Carlos III University of Madrid, Spain

³Physics of Fluids, University of Twente, The Netherlands

January 2, 2024

Abstract

We present a surface analog to a dripping faucet, where a viscous liquid slides down an immiscible meniscus. Periodic pinch-off of the dripping filament is observed, generating a succession of monodisperse floating lenses. We show that this interfacial dripping faucet can be described analogously to its single-phase counterpart, replacing surface tension by the spreading coefficient, and even undergoes a transition to a jetting regime. This liquid/liquid/gas system opens perspectives for the study of the dynamics of emulsions at interfaces.

1 Introduction

The dripping faucet has attracted scientist's attention since the times of J. C. Maxwell and Lord Rayleigh [1, 2]. One reason is because of its practical importance as a tool to generate monodisperse droplets. In fact, techniques based on the dripping faucet are used in the pharmaceutical industry, micro- and nano-technology, metallurgy, etc. to produce monodisperse droplets with sizes ranging from several microns to around the millimeter [3]. Beyond applications, the dripping faucet also turns out to be a dynamical system that encompasses stimulating and challenging fundamental problems: period doubling, chaos, dripping-to-jetting transition, etc. [1, 4].

In some of the applications mentioned above, droplets may evolve at the interface between an immiscible liquid and a gas, in which case they are called *liquid lenses* [5, 6]. Emulsions at a liquid/gas interface are involved in flotation processes [7], enhanced oil recovery [8], predicting the dispersal of oil spills [9, 10, 11], or wastewater management [12]. Despite the practical interest of those three-phase fluid systems, some of their fundamental aspects have only recently been unravelled [13, 14, 15, 16, 17, 18, 19].

Beyond the scale of single units or pairs, still very little is known on the collective dynamics of liquid lenses [20, 21], perhaps in part for a lack of large-scale generation methods. In this Letter we present a system analog to the dripping faucet, where a dispersed phase made of liquid 2 is generated directly at the surface of an immiscible, denser liquid 1. We show that this original system, dubbed *interfacial dripping faucet*, is able to periodically generate monodisperse liquid lenses in a controlled fashion, and we rationalize the volume of the produced lenses.

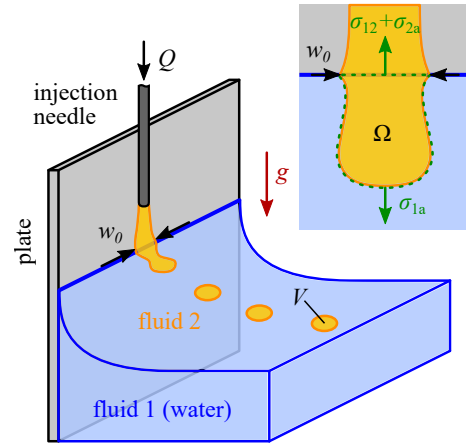


Figure 1: (a) Geometry of the interfacial dripping faucet. (b) Capillary forces exerted on a control volume Ω of liquid 2, as it enters the meniscus region (blue).

2 System description

Geometry The interfacial dripping faucet geometry is pictured in Fig. 1. A perfectly wetting vertical plate is partially dipped into a bath of liquid 1, which forms a meniscus. An injection needle placed vertically against the plate injects liquid 2 at a constant flow rate Q . Liquid 2 forms a rivulet flowing down the dry substrate until it meets the three-phase contact line between the plate and the meniscus of liquid 1. Downstream, a floating ligament of liquid 2 forms at the surface of liquid 1. The fate of this ligament, of width w_0 at the contact line, depends on the liquid properties and flow conditions.

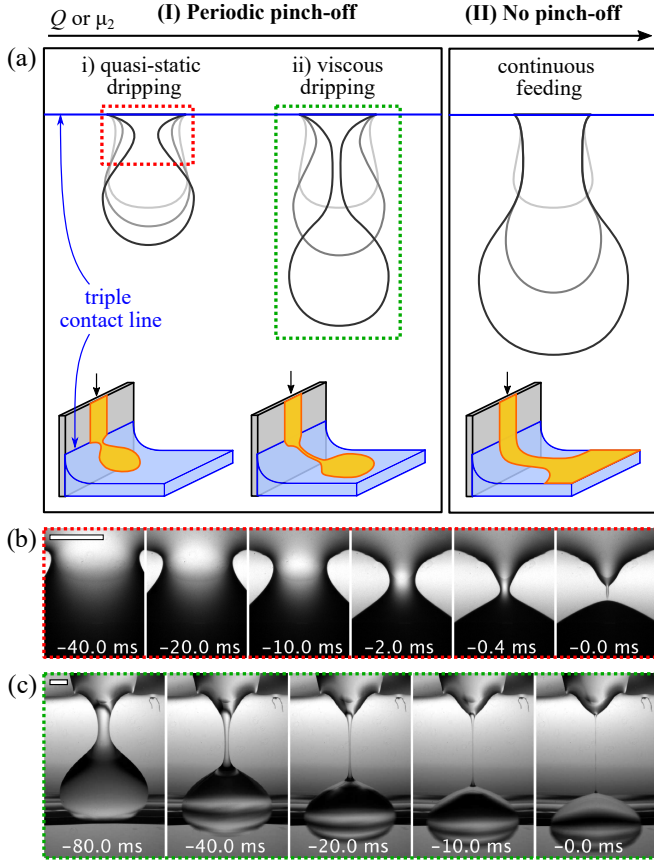


Figure 2: (a) Regimes of the interfacial dripping faucet. The top sketches qualitatively represent the contour of the floating ligament (front view) at different times, increasing from lighter to darker shade. The bottom sketches show an angled view of the floating ligament on the water meniscus. (b) Experimental time sequence of pinch-off for dodecane with $Q = 5 \mu\text{L}/\text{min}$ (quasi-static dripping, i). (c) Time sequence of pinch-off for S200 mineral oil, $Q = 50 \mu\text{L}/\text{min}$ (viscous dripping, ii). Both scale bars are $500 \mu\text{m}$.

Liquids In our experiments, liquid 1 is ultrapure water, with density $\rho_1 = 998 \text{ kg}/\text{m}^3$, dynamic viscosity $\mu_1 = 0.98 \text{ mPa}\cdot\text{s}$ and surface tension $\sigma_{1a} = 72 \text{ mN}/\text{m}$ in our room conditions ($T = 21 \text{ }^\circ\text{C}$). Six different alkanes and mineral oils, all lighter than water, are used as the dispersed phase (liquid 2). Those liquids have similar densities ρ_2 , surface tensions σ_{2a} and interfacial tensions with water σ_{12} , but dynamic viscosities μ_2 spanning almost 4 decades ($1.5 \text{ mPa}\cdot\text{s}$ for dodecane to $7571 \text{ mPa}\cdot\text{s}$ for mineral oil RTM30, see Appendix A). The spreading parameter $\mathcal{S} = \sigma_{1a} - (\sigma_{12} + \sigma_{2a})$ and the cloaking parameter $\mathcal{C} = \sigma_{2a} - (\sigma_{12} + \sigma_{1a})$ of all those liquid pairs are negative, meaning that liquid 2 is able to form stable and unclashed lenses on a water bath (see Appendix A).

Phenomenology Depending on the viscosity μ_2 and the injection flow rate Q (varied from 1 to $500 \mu\text{L}/\text{min}$) of the dispersed phase, two regimes can be observed (Fig. 2a). In the first regime (I), found for small values of Q and/or

μ_2 , the floating ligament of liquid 2 pinches off periodically, leading to the formation of identical liquid lenses that “drip” along the water meniscus (Movie S1). This periodic dripping regime remains stable as long as the injection continues, and the water surface is not entirely covered with lenses. High-speed imaging reveals that two limiting cases can be distinguished, depending on the pinch-off location and morphology. Quasi-static dripping (i) is characterized by a necking and pinch-off close to the contact line (Fig. 2b, Movie S2). In viscous dripping (ii), the floating ligament stretches into a long thread that eventually pinches off further down on the meniscus (Fig. 2c, Movie S3). Increasing the flow rate Q and the viscosity μ_2 of liquid 2, another regime (II) emerges, in which the ligament never breaks (Movie S5).

3 Periodic pinch-off regime

We first focus on characterizing the periodic pinch-off regime (I). Experimentally we acquire videos of the meniscus region, where lenses are formed and break up from the floating ligament. Once a lens has pinched off, its position x in the direction perpendicular to the plate is recorded as a function of time t using an automated in-house image processing code.

Periodicity Fig. 3a displays examples of $x-t$ trajectories of a series of lenses detached consecutively, here for dodecane injected at $Q = 50 \mu\text{L}/\text{min}$. The time at which the lens reaches a reference position ($\sim 13 \text{ mm}$ in this case) allows us to robustly measure the time interval Δt_n between lens n and the following lens $n + 1$, referred to as the dripping interval. For a given liquid and flow rate, the average value Δt of the dripping intervals will be referred to as the *dripping period* (see Appendix B).

To quantify the fluctuations of Δt_n around Δt , we plot in Fig. 3b the histogram of all the dripping intervals measured for the same experiment. A Gaussian fit (dashed curve) is performed to define the standard deviation of the dripping intervals, denoted $\sigma_{\Delta t}$. The typical variability in dripping interval, $\sigma_{\Delta t}/\Delta t$, is of the order of 5 to 10%, comparable to that observed in the classical dripping faucet in the constant-dripping interval regime [4].

In the classical dripping faucet, significant variability of the dripping interval can however be observed at large flow rates. Period doubling or chaotic dripping regimes have been reported when Δt_n is of the order of or smaller than the typical recoiling time of the filament after pinch-off [1, 22]. To assess the periodicity of the interfacial dripping faucet, we compute the time-return plot of the dripping interval in Fig. 3c. In case of period doubling, for example, one would observe two clusters of points symmetric with respect to the bisector line [4]. Here, the data is scattered around the line $\Delta t_{n+1} = \Delta t_n$ (dashed

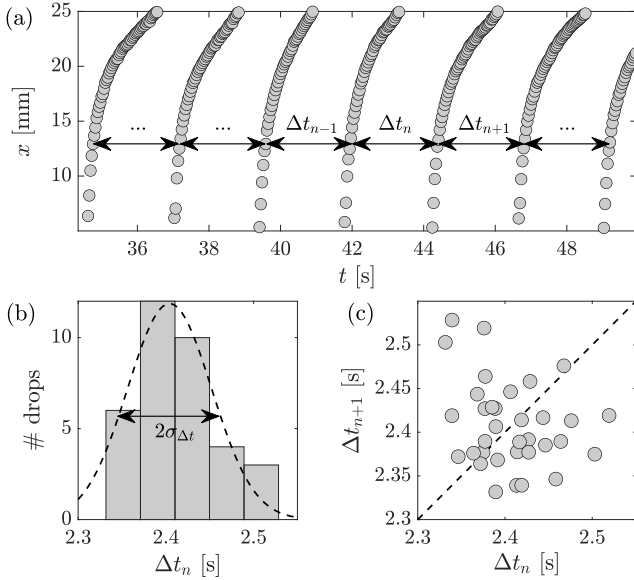


Figure 3: Periodicity assessment for a given experimental session (dodecane, $Q = 50 \mu\text{L}/\text{min}$). (a) Example of $x-t$ trajectories for several consecutive lenses, allowing us to compute the dripping intervals Δt_n . (b) Histogram of dripping intervals with its Gaussian fit (dashed curve), used to estimate the standard deviation $\sigma_{\Delta t}$. (c) Time-return plot of the dripping intervals.

line) with no particular trend, suggesting that successive dripping events are uncorrelated. This feature is observed across the whole parameter range we investigated, showing that the dripping period Δt is well-defined for the interfacial dripping faucet.

Lens volume When dripping is periodic, as demonstrated above, the volume V of the emitted lenses and the dripping period Δt are related by mass conservation, $Q = V\Delta t$. This relation holds as long as the volume of any satellite lens created at pinch-off can be neglected. Using high-speed recordings of the pinch-off, we checked that the satellites are orders of magnitude smaller than the main lens, consistently with the observations of Ref. [23].

Fig. 4a shows the lens volume V , deduced from the dripping period Δt , as function of the flow rate Q for various injected liquids, color-coded according to their viscosity. We observe that the volume grows slowly with the flow rate for a given liquid, with a more pronounced slope the more viscous the liquid is. For a 250-fold increase in flow rate Q , the lens volume V grows by a factor 3 in the case of the least viscous liquid we studied (dodecane), and by factor 5 for the much more viscous S200 mineral oil.

Quasi-static limit To rationalize this behavior we propose a mechanistic model to predict the detached lens volume, inspired by the classical dripping faucet [24, 25].

In the limit where the flow rate Q and/or viscosity μ_2 are small enough so that viscous forces can be neglected, the shape of the floating ligament is mainly set by capillarity and gravity (limit (i) in Fig. 2). Analogously to pendant drops [26], there is a certain volume V_c above which capillary forces can no longer sustain the weight of liquid 2, and the floating ligament breaks.

To determine V_c , we apply a force balance on a control volume Ω containing the injected liquid at the moment of lens detachment (see inset in figure 1a). The total capillary force exerted on Ω is $F_c \sim w_0(\sigma_{1a} - \sigma_{2a} - \sigma_{12})$. Denoting $S = \sigma_{2a} + \sigma_{12} - \sigma_{1a}$ the negative spreading parameter (such that $S > 0$), we have $F_c \sim w_0 S$. The critical volume V_c is found balancing F_c with the liquid weight in the floating filament, $\rho_2 g V_c \sim w_0 S$, where $g = 9.8 \text{ m/s}^2$ is the acceleration of gravity. This yields $V_c \sim w_0 S / \rho_2 g$, and therefore a dripping period $\Delta t^{(i)} = V_c / Q$ in limiting case (i).

Note that we restrict ourselves here to the vicinity of the triple contact line on the plate, where the water meniscus is vertical, and so is the effective gravity field. This assumption is supported in our experiments by the fact that the typical lens size $V^{1/3}$ is smaller than the water meniscus extension, of order $\ell_{c1} = \sqrt{\sigma_{1a} / \rho_1 g}$ ($0.4 \lesssim V^{1/3} / \ell_{c1} \lesssim 1$).

Viscous stretching limit In the opposite limit where the flow parameters are such that viscous forces dominate over capillary forces, the lens volume is set by the viscous stretching dynamics of the ligament (limiting case (ii) in Fig. 2). Friction due to the water substrate can be neglected as $\mu_1 \ll \mu_2$ in most of our experiments, and the shear strain rate in the bath (of size $\sim 10 \text{ cm}$) is much smaller than the longitudinal strain rate inside the ligament (of millimetric length scale w_0). Viscous stresses are then dominated by the Trouton stresses inside the ligament, like in the viscous round jet [27], rather than by the shear stresses exerted by the bath on the ligament. Exact solutions have been obtained for the classical, axisymmetric dripping faucet [25], but we focus here on scaling arguments.

Suppose that a viscous liquid is injected at $t = 0$ from a nozzle of cross-sectional area A_0 . At a time t , the weight of liquid hanging is $\rho_2 g Q t$, which induces a stretching of the ligament that is mediated by viscosity. The elongational viscous stress is $3\mu_2 \dot{\epsilon}$, where $\dot{\epsilon}$ is the stretching rate, and $3\mu_2$ the Trouton viscosity [28]. The corresponding viscous force in the ligament is $3\mu_2 \dot{\epsilon} A \sim \mu_2 \partial A / \partial t$, where A is the instantaneous ligament cross-section. Balancing this force with the lens weight, we find the typical stretching time of the ligament, $\Delta t^{(ii)} = (\mu_2 A_0 / \rho_2 g Q)^{1/2}$. The volume of the lens filled during that time therefore scales as $V \sim Q \Delta t^{(ii)} \sim (\mu_2 A_0 Q / \rho_2 g)^{1/2}$.

Collapsing the data Most experiments lie between the two limiting behaviors discussed previously. We propose

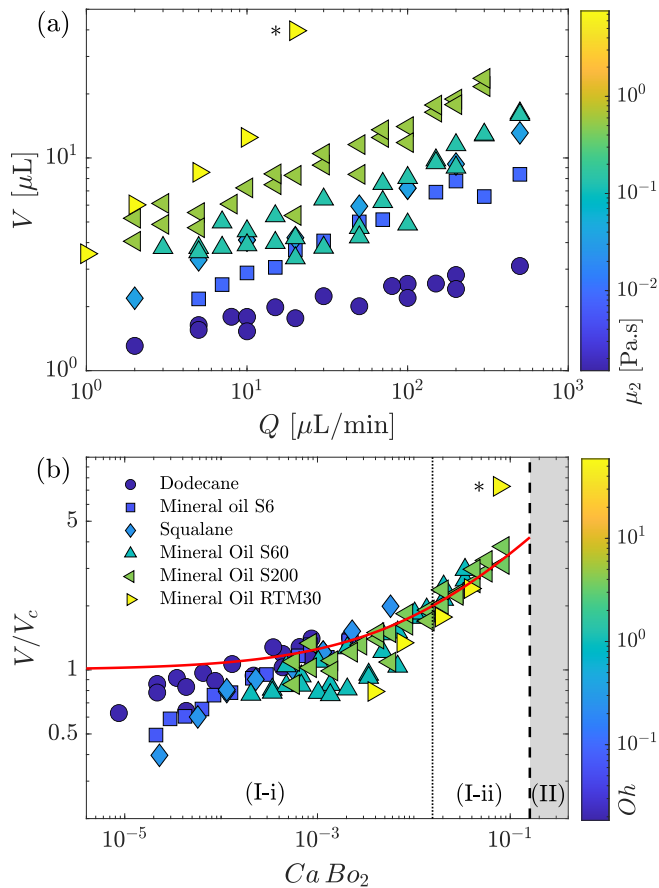


Figure 4: (a) Average liquid lens volume, $V = Q \Delta t$, as a function of the flow rate Q . The color encodes the liquid dynamic viscosity μ_2 . (b) Dimensionless lens volume V/V_c as a function of the dimensionless group Ca Bo_2 . The color encodes the Ohnesorge number $Oh = \mu_2 / \sqrt{\rho_2 g w_0}$. The solid line corresponds to equation (1) with $C = 8$. The dotted and dashed lines show the transitions between periodic behaviors (i) and (ii), and between regimes (I) and (II), respectively.

here that the dripping period is approximated by the sum of the respective predictions in the two limiting cases, *i.e.* $\Delta t = \Delta t^{(i)} + C \Delta t^{(ii)}$, with C a dimensionless numerical constant [24]. Multiplying this equation times Q/V_c , we arrive at

$$\frac{V}{V_c} = 1 + C (\text{Ca Bo}_2)^{1/2}. \quad (1)$$

We have introduced here the Bond number $\text{Bo}_2 = \rho_2 g w_0^2 / S$ of the floating ligament, and the capillary number $\text{Ca} = \mu_2 U / S$ based on the characteristic injection speed at the contact line, $U = Q / A_0$. We compute A_0 as the cross-sectional area of the ligament at the three phase contact line, deduced from the experimental value of the ligament width w_0 and the wetting properties (see Appendix C).

Fig. 4b shows the dimensionless volume V/V_c as a function of the dimensionless group Ca Bo_2 for all the liquids used in our experiments. The color encodes the Ohnesorge number, $Oh = \mu_2 / \sqrt{\rho_2 S w_0}$. The experiments

nearly collapse onto a master curve of the form given in Eq. (1) (solid line). The dotted line, corresponding to $C (\text{Ca Bo}_2)^{1/2} \sim 1$, qualitatively marks the transition from limiting behaviors i) to ii).

We find the collapse of the data quite remarkable, taken into account the simplifications of our model. First, the Ohnesorge number varies more than two orders of magnitude between the different liquids. Second, when changing liquids, not only does the Ohnesorge number changes but also, to a lesser extent, the ligament wetting properties on water (*i.e.*, Neumann angles) and the Bond number $\text{Bo}_1 = w_0^2 / \ell_{c1}^2$. Hence the agreement between the prediction of Eq. (1) and the experimental data shows the robustness of the underlying physical mechanisms.

4 No-pinch-off regime

Increasing further the flow rate and viscosity of liquid 2, experiments show the emergence of another regime (denoted (II) in Fig. 2), in which the floating ligament never breaks. The reason for the occurrence of regime (II) is that the water meniscus is curved, a fact that we ignored so far for the description of the periodic dripping regime (I). As a consequence of this curvature, the effective gravity felt by the ligament (*i.e.* the driving force promoting pinch-off) decreases as it slides down. If pinch-off has not occurred by the time the bath surface becomes horizontal and the driving force vanishes, then it never will. More quantitatively, the condition for the transition from regime (I) to (II) to happen is that the length ℓ_{po} at which the ligament would break exceeds the water meniscus length ℓ_{c1} . We can estimate the pinch-off distance as $\ell_{po} \sim U t_{po}$, with $t_{po} \sim 6\pi \mu_2 w_0 / S$ the time taken by the stretched ligament to destabilize in the absence of gravity (see Appendix C). Thus, the condition $\ell_{c1} \sim \ell_{po}$ for the onset of regime (II) is expressed as $6\pi \text{Ca Bo}_1^{1/2} \sim 1$ or equivalently, $\text{Ca Bo}_2 \sim \text{Bo}_2 / 6\pi \text{Bo}_1^{1/2} \approx 0.16$, roughly the same for all liquids.

This threshold, plotted as a dashed line in Fig. 4b, is consistent with the experimental data. Movie S4, corresponding to RTM30 and $Q = 20 \mu\text{L}/\text{min}$ ($6\pi \text{Ca Bo}_1^{1/2} = 0.45$), illustrates the transition towards pinch-off suppression: the ligament wobbles several times before eventually breaking. This delayed yet still periodic pinch-off translates into a very large lens volume (point marked with an asterisk in Fig. 4), which stands out of the experimental trend as it is close to the (I)-(II) transition. Increasing further the flow rate ($Q = 50 \mu\text{L}/\text{min}$, corresponding to $6\pi \text{Ca Bo}_1^{1/2} = 1.13$), pinch-off is totally suppressed. As illustrated in Movie S5, the ligament continuously feeds a floating puddle of liquid 2 as long as injection continues.

5 Conclusion

In summary, we explore the physics of forced liquid dripping along an immiscible liquid/air interface, in partial wetting conditions. This three-phase configuration, dubbed “interfacial dripping faucet”, exhibits a periodic pinch-off regime in a wide range of control parameters, leading to the generation of monodisperse liquid lenses. Both the critical volume and the dripping period are found to follow analogous laws to the free, axisymmetric dripping faucet [25, 27], but with a key difference: the surface tension of the injected liquid must be replaced by the negative spreading coefficient, S . This accounts for the fact that the surface tension of the bath/air interface does not contribute to keep a lens confined but, on the contrary, pulls to spread it. Beyond analogies, the interfacial dripping faucet also reveals an original regime not observed in a free vertical dripping faucet. For sufficiently large viscosity and flow rate of the dispersed phase, pinch-off is suppressed altogether and the liquid ligament continuously feeds a floating puddle.

A very important control parameter of the interfacial dripping faucet is the geometry of the meniscus, which is itself governed by the plate geometry and wettability. A steeper meniscus could translate into a delayed no-dripping regime, a thinner ligament (and hence smaller lenses) or even in the appearance of multiple dripping periods or a continuous jetting regime. The interfacial dripping faucet opens new perspectives to generate two-dimensional emulsions in the absence of confining walls [29, 30] and, more generally, to study the fundamentals of liquid/liquid/gas dispersions, at play in many industrial and natural settings [7, 8, 9, 10, 11, 12].

Acknowledgments

J.R.R. acknowledges funding from the Spanish MCIN/AEI/10.13039/501100011033 through Grant No. PID2020-114945RB-C21. This project has received funding from the European Union’s Horizon 2020 research and innovation programme under the Marie Skłodowska-Curie grant agreement No 882429 (L.C.). V.B and J. H. S. acknowledge financial support from NWO through the VICI Grant No. 680-47-632.

A Materials and methods

A.1 Liquid properties

For all experiments, the liquid substrate (liquid 1) is ultrapure water (Milli-Q) of surface tension $\sigma_{1a} = 72$ mN/m. Six different liquids are used as the dispersed phase (liquid 2): dodecane (99 %, Acros Organics), squalane (99 %, Thermo Fisher), and mineral oils S6, S60, S200 and RTM30 (Paragon Scientific Ltd), all used as received. Table 1 summarizes the properties of

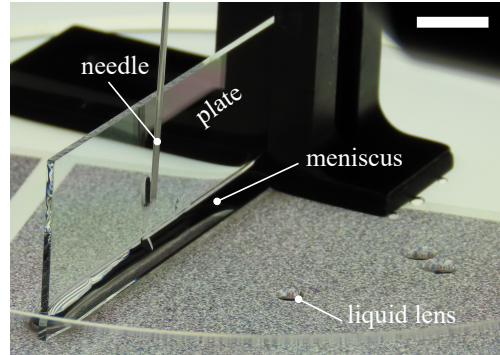


Figure 5: Picture of the experimental configuration, where a random dot pattern underneath the bath is used to ease lens visualization. The scale bar is 1 cm.

those liquids, as reported in the literature, as well as the deduced spreading parameter $\mathcal{S} = \sigma_{1a} - (\sigma_{12} + \sigma_{2a})$ and cloaking parameter $\mathcal{C} = \sigma_{2a} - (\sigma_{12} + \sigma_{1a})$.

A.2 Experimental setup and protocol

Solid and liquid substrates An experimental realization of the interfacial dripping faucet geometry is shown in Fig. 5. In all our experiments, the plate is a microscope glass slide (dimensions 25 cm \times 75 cm), about 1 mm in thickness. Before use, glass slides are left to clean for 15 minutes in acetone in an ultrasound bath, then rinsed with ethanol, ultrapure water and isopropanol, and then dried with an air gun. Finally, the clean slide is hydrophilized in a plasma cleaner to make sure that it is perfectly wetted by water. We performed a control experiment with a clean non-hydrophilized glass slide (*i.e.* having undergone the above cleaning procedure, but not the hydrophilization step), with water contact angle of about 15°. The dripping period showed no appreciable difference compared to the hydrophilic case.

This plate is held vertically by two right-angle brackets (Thorlabs) inside a disposable Petri dish (diameter 150 mm, polystyrene). The holders are previously cleaned using the same procedure as for the glass slides. Ultrapure water is then gently poured into the Petri dish, forming a meniscus against the plate, until the water bath reaches a depth of at least 5 mm.

Injection system The dispersed phase (liquid 2) is loaded in a 1 mL glass syringe (Hamilton), connected to a stainless steel needle (Hamilton) by PEEK tubings and connectors. Liquid 2 is steadily injected in this system by a syringe pump (Harvard Apparatus), delivering a constant flow rate Q in the range $Q = 1 - 500$ $\mu\text{L}/\text{min}$. In all the experiments but one, the needle gauge is G21 (514 μm inner diameter, 819 μm outer diameter). We also perform an additional experiment with a G27 needle (210 μm inner diameter, 413 μm outer diameter). For a given liquid, the dripping period did not change substan-

Liquid 2	Refs.	ρ_2	μ_2	σ_{2a}	σ_{12}	\mathcal{S}	\mathcal{C}	α_{12}	α_{2a}
		[kg/m ³]	[mPa·s]	[mN/m]	[mN/m]	[mN/m]	[mN/m]	[rad]	[rad]
dodecane	[31, 32]	750	1.5	25	53	-6	-100	0.264	0.586
S6	[33]	832	8.7	31	54	-13	-95	0.408	0.762
squalane	[34, 35, 36]	810	35	31	56	-15	-97	0.421	0.831
S60	[33]	863	135	31	54	-13	-95	0.408	0.762
S200	[33]	863	563	31	54	-13	-95	0.408	0.762
RTM30	[33]	868	7571	31	54	-13	-95	0.408	0.762

Table 1: Physical properties of the fluids used as the dispersed phase (liquid 2) at room temperature $T \sim 21$ °C: density ρ_2 , dynamic viscosity μ_2 , surface tension σ_{2a} and interfacial tension σ_{12} with water. We also show the deduced spreading parameter \mathcal{S} , cloaking parameter \mathcal{C} , and Neumann angles α_{2a} and α_{12} , calculated from Eqs. (4).

tially when changing the needle gauge from G21 to G27. The needle is held in place vertically, leaning against the plate, with its tip at a distance $\Delta z \approx 6 - 8$ mm above the surface of the undeformed bath (see Fig. 6a).

When changing to a different dispersed phase, the whole injection system (syringe, tubing, fittings, needle) is flushed with chloroform and then acetone. The syringe, fittings and needle are then dismantled and soaked in chloroform for about 10 minutes, along with the right-angle holders. These components are subsequently sonicated in acetone for 15 minutes and finally rinsed with ethanol, ultrapure water and isopropanol, before being dried with an air gun. When the phase to be cleaned is dodecane, chloroform is simply substituted by acetone.

Imaging system The interfacial dripping faucet is illuminated from below with a uniform white light panel, as sketched in Fig. 6a. During dripping, a camera (Ximea) records a front view at a frame rate between 6 and 60 fps, depending on the flow conditions.

The optical index contrast between liquids 1 and 2 is typically small. To facilitate the visualization and automatic detection of the lenses, we therefore place a speckled background under the water bath (see picture in Fig. 5). It consists of a random dot pattern with black area fraction of 50%, laser-printed at 1200 dpi on a transparent plastic sheet. Before injection of liquid 2 starts, we take a picture of this background that will serve as a reference for image processing (see section B).

For adequate visualization of the curved meniscus, the camera is inclined at an angle of about 30° with respect to the horizontal direction. This introduces a perspective effect that has to be subsequently corrected. To do so, we acquire an image of a horizontal, square calibration grid, in the absence of the water-filled bath. This calibration snapshot will be used in the image processing to compute the transformation matrix that would make the angles between the grid lines right (see section B).

For a reduced set of experiments, we also visualize the pinch-off dynamics of the dripping ligament with a high-speed camera (Photron Nova S12) equipped with a microscopic lens (Navitar x12 zoom lens). The frame rate is set between 15 and 50 kfps, depending on the flow

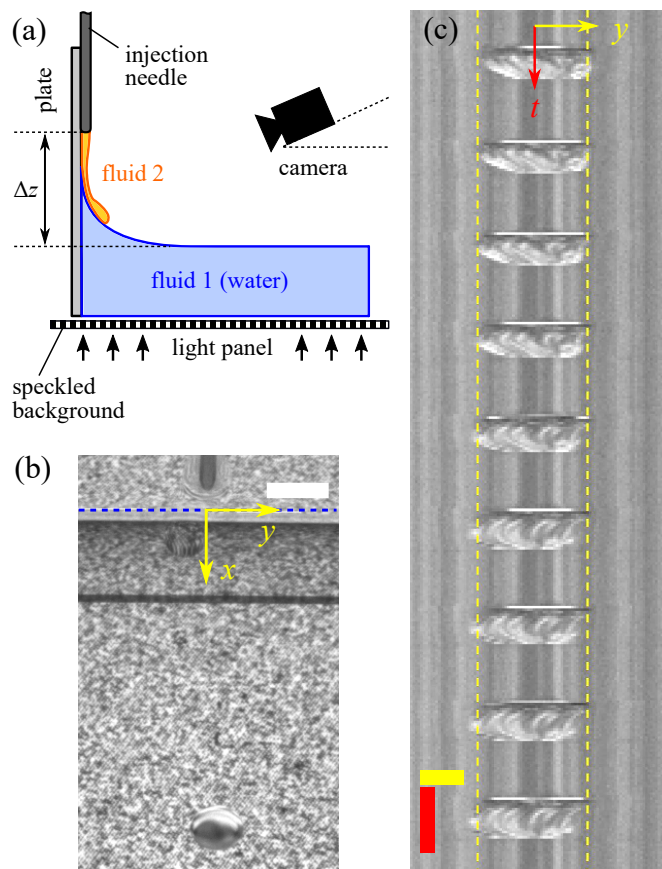


Figure 6: (a) Sketch of the imaging configuration of the interfacial dripping faucet. — (b) Snapshot of a movie corresponding to a dodecane experiment, with $Q = 100$ $\mu\text{L}/\text{min}$. The blue dashed line marks the location of the contact line. At the bottom of the snapshot we see the previously detached lens. The scale bar is 5 mm. — (c) Zoomed time-space diagram at the contact line (blue dashed line in panel (b)). The yellow dashed lines mark the maximum width w_0 of the ligament at the contact line. The y scale bar (yellow) is 1 mm, while the time scale bar (red) is 1 s.

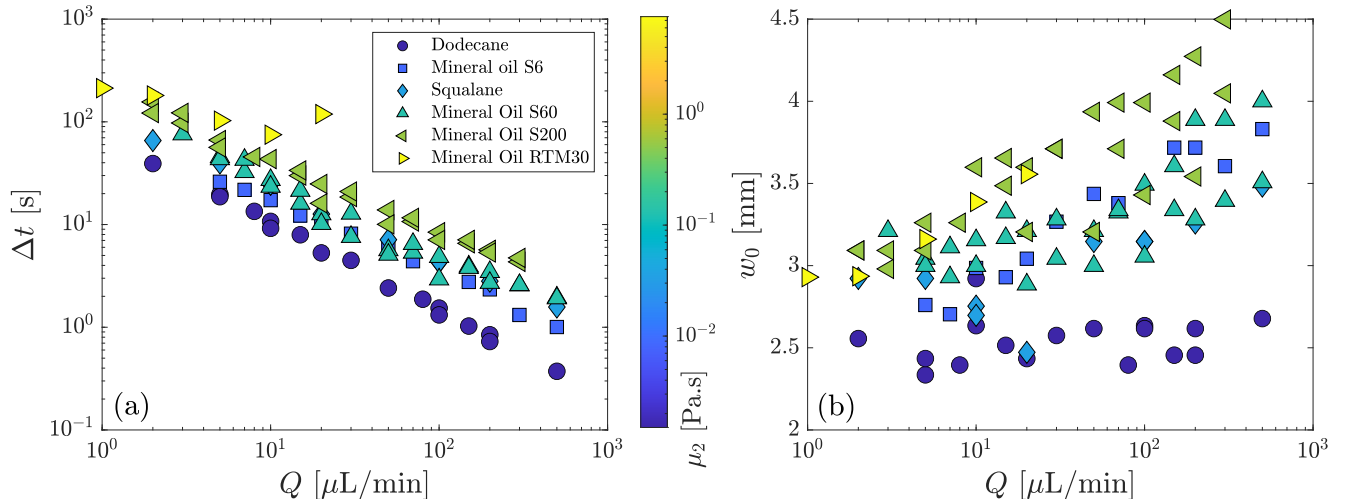


Figure 7: (a) Dripping period Δt and (b) ligament maximum width at the contact line, w_0 , as a function of the flow rate Q for different injected liquids. The color corresponds to the dynamic viscosity μ_2 .

parameters. Examples of resulting image sequences are presented in Fig.2b and c of the main text.

B Image processing

In this section, we explain how the acquired videos are processed to measure two magnitudes of interest: the dripping interval, Δt , and the dripping ligament width at the contact line, w_0 .

B.1 Dripping interval Δt

We detect the time evolution of the position of the liquid lenses, once detached from the feeding rivulet, by digital processing of images like that shown in Fig. 6b. The algorithm, implemented by a house-made code written in MATLAB[©] 2020a, consists in applying the following steps to all the images of a video:

1. The reference speckled background image is subtracted.
2. The resulting image is corrected for perspective effects using the transformation matrix obtained from the image of the calibrated grid.
3. The transformed image is binarized using a gray-level threshold.
4. A morphological closing operation is applied to the binary image.
5. Objects larger than a threshold size are detected, in particular recording the location of their centers as a function of time.

After the images are processed, a home-made tracking algorithm is applied to detect the trajectories of individual lenses. Finally, we define the dripping interval of lens

number n , Δt_n , as the interval between the time when the lens crosses a given position (at about two capillary lengths from the contact line) and when the next lens crosses the same position (figure 3a in main text). Then, we compute the dripping period as the mean dripping interval

$$\Delta t = \frac{1}{N} \sum_{n=1}^N \Delta t_n, \quad (2)$$

where N is the total number of lens. The dripping periods obtained applying this procedure to all the movies are shown in Fig. 7a.

B.2 Ligament width w_0

The main lengthscale we use to describe the production of liquid lenses is the dripping ligament width w_0 at the contact line. This magnitude is not trivial to measure directly from the images, especially when liquid 2 is not very viscous. In this parameter range, the injected liquid recoils right after pinch-off, and no ligament can therefore be seen at the contact line during part of the dripping process. This is for instance the case in the example shown in Fig. 6b.

Given this limitation, the *maximum* ligament width at the contact line is the only observable can be consistently obtained for all the experimental conditions. We will therefore use it as the definition of w_0 . To measure it, we extract the slice (*i.e.* pixel line) corresponding to the contact line in each frame of the video. All those slices make up a synthetic time-space diagram (Fig. 6c), where the m -th column contains the slice from the m -th image. An automated computer algorithm is then used to detect the maximum width of the ligament in this synthetic image (dashed yellow lines in Fig. 6c). We show in Fig. 7b the evolution of w_0 for different flow rates and Ohnesorge numbers.

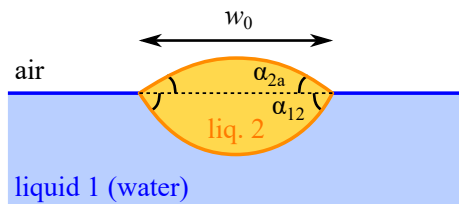


Figure 8: Simplified cross-section geometry of the floating ligament of liquid 2, downstream the contact line.

C Modelling the floating ligament

C.1 Geometry

The Neumann angles α_{2a} and α_{12} formed by the top (liquid 2 / air) and bottom (liquid 1 / liquid 2) interfaces of a liquid lens or ligament are computed from the force balance at the triple contact line liquid 1 / liquid 2 / air [14]:

$$\sigma_{2a} \sin \alpha_{2a} - \sigma_{12} \sin \alpha_{12} = 0, \quad (3)$$

$$\sigma_{2a} \cos \alpha_{2a} + \sigma_{12} \cos \alpha_{12} = \sigma_{1a}. \quad (4)$$

These angles are used to compute the cross-sectional area of the ligament downstream the bath-solid contact line using the simplified geometry described below.

Knowing the ligament width w_0 , the cross-sectional area downstream the contact line, A_0 , is computed assuming a simplified geometry consisting of two circular arcs that form Neumann angles α_{2a} and α_{12} with respect to a horizontal bath surface (see figure 8). Under these assumptions, the cross-sectional area of the ligament is given by

$$A_0 = \frac{w_0^2}{2} \left(\frac{\alpha_{12}}{\sin^2 \alpha_{12}} - \frac{1}{\tan \alpha_{12}} + \frac{\alpha_{2a}}{\sin^2 \alpha_{2a}} - \frac{1}{\tan \alpha_{2a}} \right). \quad (5)$$

C.2 Pinch-off time in the absence of gravity

To estimate the pinch-off time of our floating ligament when it is on the horizontal part of the bath we make the assumption that it can be treated as a free circular viscous cylinder. Doing so, we can apply the calculations done in §111 of Chandrasekhar [37]. Adapting their equation (106) to our notation, the perturbed ligament width is expressed as

$$w(x, t) = w_0 + \varepsilon_0 \exp[-i(\omega t - kx)], \quad (6)$$

where w_0 is the unperturbed ligament width, ε_0 the perturbation amplitude, $k = 2\pi/\lambda$ the angular wave number corresponding to a wavelength λ and ω the angular frequency. For very viscous fluids, the imaginary part of the angular frequency is given by (Equation 161)

$$\omega_i = \frac{S}{3\mu_2 w_0} \left[1 - \left(\frac{k w_0}{2} \right)^2 \right]. \quad (7)$$

The fastest-growing mode of the Rayleigh-Plateau instability is that that maximizes ω_i , which occurs in the limit of very long waves, $k w_0 \ll 1$. Denoting the pinch-off time as the growth time of this fastest-growing perturbation we obtain finally

$$t_{po} = \frac{2\pi}{\omega_i} = \frac{6\pi\mu_2 w_0}{S}. \quad (8)$$

References

- [1] C. Clanet and J. C Lasheras. Transition from dripping to jetting. *Journal of Fluid Mechanics*, 383:307–326, 1999.
- [2] J. Eggers and E. Villermaux. Physics of liquid jets. *Reports on Progress in Physics*, 71(3):036601, 2008.
- [3] J. M. Montanero and A. M. Gañán-Calvo. Dripping, jetting and tip streaming. *Reports on Progress in Physics*, 83(9):097001, aug 2020.
- [4] H. J. Subramani, H. K. Yeoh, R. Suryo, Q. Xu, B. Ambravaneswaran, and O. A. Basaran. Simplicity and complexity in a dripping faucet. *Physics of Fluids*, 18(3):032106, 2006.
- [5] R. E. Johnson and S. S. Sadhal. Fluid mechanics of compound multiphase drops and bubbles. *Annual Review of Fluid Mechanics*, 17(1):289–320, 1985.
- [6] A. Nepomnyashchy. Droplet on a liquid substrate: Wetting, dewetting, dynamics, instabilities. *Current Opinion in Colloid & Interface Science*, 51:101398, 2021.
- [7] L. Su, Z. Xu, and J. Masliyah. Role of oily bubbles in enhancing bitumen flotation. *Minerals Engineering*, 19:641–650, 05 2006.
- [8] W. R. Rossen. Foams in enhanced oil recovery. In *Foams*, pages 413–464. Routledge, 2017.
- [9] J. M. Shaw. A microscopic view of oil slick breakup and emulsion formation in breaking waves. *Spill science & technology bulletin*, 8(5-6):491–501, 2003.
- [10] I. D. Nissanka and P. D. Yapa. Oil slicks on water surface: Breakup, coalescence, and droplet formation under breaking waves. *Marine pollution bulletin*, 114(1):480–493, 2017.
- [11] I. D. Nissanka and P. D. Yapa. Calculation of oil droplet size distribution in ocean oil spills: A review. *Marine pollution bulletin*, 135:723–734, 2018.
- [12] R. K. Gupta, G. J. Dunderdale, M. W. England, and A. Hozumi. Oil/water separation techniques: a review of recent progresses and future directions. *Journal of Materials Chemistry A*, 5(31):16025–16058, 2017.

- [13] J. Sebilliau. Equilibrium thickness of large liquid lenses spreading over another liquid surface. *Langmuir*, 29(39):12118–12128, 2013.
- [14] P. D. Ravazzoli, A. G. Gonzalez, J. A. Diez, and H. A. Stone. Buoyancy and capillary effects on floating liquid lenses. *Physical Review Fluids*, 5(7):073604, 2020.
- [15] M. A. Hack, W. Tewes, Q. Xie, C. Datt, K. Harth, J. Harting, and J. H. Snoeijer. Self-similar liquid lens coalescence. *Physical Review Letters*, 124(19):194502, 2020.
- [16] W. Tewes, M. A. Hack, C. Datt, G. G. Peng, and J. H. Snoeijer. Theory for the coalescence of viscous lenses. *Journal of Fluid Mechanics*, 928:A11, 2021.
- [17] T. Scheel, Q. Xie, M. Sega, and J. Harting. Viscous to inertial coalescence of liquid lenses: A lattice boltzmann investigation. *Physical Review Fluids*, 8(7):074201, 2023.
- [18] F. Wodlei, J. Sebilliau, J. Magnaudet, and V. Pimienta. Marangoni-driven flower-like patterning of an evaporating drop spreading on a liquid substrate. *Nature communications*, 9(1):820, 2018.
- [19] B. Reichert, J.-B. Le Cam, A. Saint-Jalmes, and G. Pucci. Self-propulsion of a volatile drop on the surface of an immiscible liquid bath. *Physical Review Letters*, 127(14):144501, 2021.
- [20] L. Keiser, H. Bense, P. Colinet, J. Bico, and E. Reyssat. Marangoni bursting: evaporation-induced emulsification of binary mixtures on a liquid layer. *Physical Review Letters*, 118(7):074504, 2017.
- [21] A. Agrawal, M. Gopu, R. Mukherjee, and D. Mampallil. Microfluidic droplet cluster with distributed evaporation rates as a model for bioaerosols. *Langmuir*, 38(15):4567–4577, 2022.
- [22] P. Coulet, L. Mahadevan, and C. S. Riera. Hydrodynamical models for the chaotic dripping faucet. *Journal of Fluid Mechanics*, 526:1–17, 2005.
- [23] J. C. Burton and P. Taborek. Role of dimensionality and axisymmetry in fluid pinch-off and coalescence. *Phys. Rev. Lett.*, 98:224502, May 2007.
- [24] R. Clift, J.R. Grace, and M.E. Weber. *Bubbles, Drops, and Particles*. Dover Civil and Mechanical Engineering Series. Dover Publications, 2005.
- [25] S. D. R. Wilson. The slow dripping of a viscous fluid. *Journal of Fluid Mechanics*, 190:561–570, 1988.
- [26] P.-G. Gennes, F. Brochard-Wyart, D. Quéré, et al. *Capillarity and wetting phenomena: drops, bubbles, pearls, waves*. Springer, 2004.
- [27] J. Eggers and T. F. Dupont. Drop formation in a one-dimensional approximation of the navier–stokes equation. *Journal of Fluid Mechanics*, 262:205–221, 1994.
- [28] P. Howell. *Extensional thin layer flows*. University of Oxford, Mathematical Institute, 1994.
- [29] K. W. Desmond, P. J. Young, D. Chen, and E. R. Weeks. Experimental study of forces between quasi-two-dimensional emulsion droplets near jamming. *Soft Matter*, 9(12):3424–3436, 2013.
- [30] B. Dollet, A. Scagliarini, and M. Sbragaglia. Two-dimensional plastic flow of foams and emulsions in a channel: experiments and lattice boltzmann simulations. *Journal of Fluid Mechanics*, 766:556–589, 2015.
- [31] D. J. Luning Prak, S. M. Alexandre, J. S. Cowart, and P. C. Trulove. Density, viscosity, speed of sound, bulk modulus, surface tension, and flash point of binary mixtures of n-dodecane with 2, 2, 4, 6, 6-pentamethylheptane or 2, 2, 4, 4, 6, 8, 8-heptamethylnonane. *Journal of Chemical & Engineering Data*, 59(4):1334–1346, 2014.
- [32] A. Goebel and K. Lunkenheimer. Interfacial tension of the water/n-alkane interface. *Langmuir*, 13(2):369–372, 1997.
- [33] K. Takamura, H. Fischer, and N. R. Morrow. Physical properties of aqueous glycerol solutions. *Journal of Petroleum Science and Engineering*, 98:50–60, 2012.
- [34] V. I. Korotkovskii, A.V. Lebedev, O.S. Ryshkova, M. F. Bolotnikov, Y. E. Shevchenko, and Y. A. Neruchev. Thermophysical properties of liquid squalane c₃₀h₆₂ within the temperature range of 298.15–413.15 k at atmospheric pressure. *High Temperature*, 50(4):471–474, 2012.
- [35] María J.P. Comuñas, X. Paredes, Félix M. Gaciño, J. Fernández, J.-P. Bazile, C. Boned, J.-L. Daridon, G. Galliero, J. Pauly, K. R. Harris, et al. Reference correlation of the viscosity of squalane from 273 to 373 k at 0.1 mpa. *Journal of Physical and Chemical Reference Data*, 42(3), 2013.
- [36] S. Goossens, D. Seveno, R. Rioboo, A. Vaillant, J. Conti, and J. De Coninck. Can we predict the spreading of a two-liquid system from the spreading of the corresponding liquid–air systems? *Langmuir*, 27(16):9866–9872, 2011.
- [37] R. Chandrasekhar. *Hydrodynamic and hydromagnetic stability*. Dover Publications, 1981.